International Journal of Heat and Mass Transfer 52 (2009) 1326–1336

Contents lists available at ScienceDirect

International Journal of Heat and Mass Transfer

journal homepage: www.elsevier.com/locate/ijhmt

Experimental and numerical investigation of natural convection effects on confined impinging jet heat transfer

M.F. Koseoglu [a], S. Baskaya [b,*]

[a] Department of Mechanical Engineering, Pamukkale University, 20070 Kınıklı, Denizli, Turkey
[b] Department of Mechanical Engineering, Gazi University, 06570 Maltepe, Ankara, Turkey

ARTICLE INFO

Article history:
Received 9 July 2007
Received in revised form 10 July 2008
Available online 12 November 2008

Keywords:
Confined impinging jets
Natural convection
Electronic cooling
CFD
LDA

ABSTRACT

The influence of natural convection on the local and average heat transfer at increasing temperature differences between the jet and the target plate from confined impinging jets has been experimentally and numerically investigated. Local Nusselt numbers were obtained numerically for jet Reynolds numbers in the range of 250–1000, and jet to target spacings of 2, 4, 8, 12 jet diameters at various modified Grashof numbers, to determine the effect of buoyancy induced natural convection. To determine the overall effect of natural convection on the average heat transfer, experiments have been conducted for Re numbers in the range 250–5000 and dimensionless jet to target spacing 2, 4, 6, 8, and 12 at increasing modified Grashof numbers. It has been determined that buoyancy induced natural convection might have opposing or assisting influence on local heat transfer at different locations of the target plate. It has also been shown that especially at low jet inlet velocities the average heat transfer coefficient at the highest modified Grashof number, where the natural convection is effective, is higher than the value corresponding to the lowest Grashof number at which buoyancy effects are negligible, by as much as 37%.

1. Introduction

Impinging jets have been widely used in industry where localized heating or cooling is required. Application areas include electronics equipment and gas turbine blade cooling, glass tempering, metal cutting, paper and cereal drying. Depending on the above applications a very broad range of temperatures and velocities are of interest.

Due to the many industrial applications of impinging jets extensive prior research has been conducted to understand their flow and heat transfer characteristics. The results from this research have been summarized by Viskanta and Jambunathan et al. [1,2]. Gardon and Akfirat have investigated the dependence of heat transfer on parameters such as Reynolds number, jet to target plate distance and turbulence for the range of *Re* numbers 450–22000 and dimensionless jet to plate distances 1/3-80 [3,4]. The flow field in confined jets has been shown to be very different from that of unconfined jets. Garimella in a review paper presented a detailed discussion of heat transfer and flow fields in confined jet impingement [5].

Impinging jets were also the subject of many numerical studies. The flow and heat transfer characteristics of laminar impinging rectangular slot jets were investigated by Sezai and Mohamed [6]. The effect of jet velocity profiles on the flow and thermal fields of laminar confined and swirling jets were investigated by Shuja et al. [7].

Temperature difference between the jet and target plate is effective on flow and heat transfer characteristics. Yu and Monkewitz [8] investigated the effect of density difference between the heated jet and the environment air and determined the self oscillating flows for the density ratios less than 0.9. In the numerical study with turbulent impinging jets Shi et al. [9] investigated the effect of large temperature difference on impingement heat transfer.

It has been stated that when the temperature difference between the jet and the target plate is less than 15 °C natural convection effects are negligible [10,11].

From the above literature review, one can see that only little information can be found in the literature for natural convection effects on impinging jet heat transfer. The present study aims to numerically and experimentally investigate buoyancy induced natural convection effects which can cause considerable changes on heat transfer at high temperature differences and low jet velocities.

2. Mathematical formulation and numerical model

In this section description of the problem under investigation is given, mathematical formulation, boundary conditions and solution methodology have been shortly described.

* Corresponding author. Tel.: +90 312 2317400x2421; fax: +90 312 2308434.
E-mail address: baskaya@gazi.edu.tr (S. Baskaya).

0017-9310/$ - see front matter © 2008 Elsevier Ltd. All rights reserved.
doi:10.1016/j.ijheatmasstransfer.2008.07.051

Nomenclature

a, b	correlation constants
A_s	heat source surface area, m^2
D	jet diameter,
F	dimensionless radiation view factor
G	gravitational acceleration, m/s^2
Gr^*	dimensionless modified Grashof number, $Gr^* = \frac{g\beta q_c L^4}{k_{air}\nu_{air}^2}$
h_{ave}	average heat transfer coefficient
H/D	dimensionless jet to target plate distance
I	electrical current
k	thermal conductivity, W/mK
L	characteristic length of the target surface, $L = A_s/P$
Nu	local Nusselt number
Nu_{ave}	average Nusselt number
p	pressure
P	perimeter of the target surface, m
Pr	Prandtl number $Pr = c_{p_{air}}\mu_{air}/k_{air}$
q_c	convection heat flux, W/m^2
Q_c	convection heat transfer rate, W
Q_{cond}	conduction heat transfer rate, W
Q_r	radiation heat transfer rate, W
Q_t	total power dissipation, W
Re	Reynolds number, $Re = (W_{in}D)/\nu_{air}$
Ri	Richardson number
s	source term
T	temperature, °C
T_j	jet inlet temperature
$T_{s,ave}$	average surface temperature, °C
T_∞	temperature of the surroundings
u, v, w	velocity components in x, y, z directions
V	voltage, V
W_{in}	jet inlet velocity, m/s
x/D	dimensionless distance from impinging point

Greek symbols

ρ	density, kg/m^3
ρ_0	reference density, kg/m^3
β	thermal expansion coefficient, 1/K
ε	heater surface emissivity
μ	dynamic viscosity, kg/ms
ν	kinematic viscosity, m^2/s
σ	Stefan-Boltzmann constant, W/m^2K^4

Subscripts

air	air
ave	average
in	inlet
s	target surface

2.1. Problem description

A schematic drawing of the confined impinging jet configuration under investigation and the actual computational domain used for the numerical simulations is shown in Fig. 1. Because of symmetry, solutions were obtained for only one quarter of the domain shown with dashed lines.

2.2. Governing equations

The equations governing 3-D steady, laminar flow of air with constant properties, except for density which is calculated by making an ideal gas assumption, can be written in the Cartesian coordinate system as follows:

Conservation of mass:

$$\frac{\partial(\rho u)}{\partial x}+\frac{\partial(\rho v)}{\partial y}+\frac{\partial(\rho w)}{\partial z}=0 \tag{1}$$

Conservation of momentum:

$$u\frac{\partial(\rho u)}{\partial x}+v\frac{\partial(\rho u)}{\partial y}+w\frac{\partial(\rho u)}{\partial z}=-\frac{\partial p}{\partial x}+\mu\left[\frac{\partial^2 u}{\partial x^2}+\frac{\partial^2 u}{\partial y^2}+\frac{\partial^2 u}{\partial z^2}\right] \tag{2}$$

$$u\frac{\partial(\rho v)}{\partial x}+v\frac{\partial(\rho v)}{\partial y}+w\frac{\partial(\rho v)}{\partial z}=-\frac{\partial p}{\partial y}+\mu\left[\frac{\partial^2 v}{\partial x^2}+\frac{\partial^2 v}{\partial y^2}+\frac{\partial^2 v}{\partial z^2}\right] \tag{3}$$

$$u\frac{\partial(\rho w)}{\partial x}+v\frac{\partial(\rho w)}{\partial y}+w\frac{\partial(\rho w)}{\partial z}=-\frac{\partial p}{\partial z}+\mu\left[\frac{\partial^2 w}{\partial x^2}+\frac{\partial^2 w}{\partial y^2}+\frac{\partial^2 w}{\partial z^2}\right]+g(\rho-\rho_a) \tag{4}$$

Conservation of energy:

$$u\frac{\partial(\rho T)}{\partial x}+v\frac{\partial(\rho T)}{\partial y}+w\frac{\partial(\rho T)}{\partial z}=\frac{\mu}{Pr}\left[\frac{\partial^2 T}{\partial x^2}+\frac{\partial^2 T}{\partial y^2}+\frac{\partial^2 T}{\partial z^2}\right]$$

The Boussinesq approximation could not be applied in this study. Gray and Giorgini [12] showed that the error due to using the Boussinesq approximation is less than 10% for air as long as $\Delta T \leqslant 28.6$ °C. However, in the present simulations temperature differences were much higher in most cases.

2.3. Solution algorithm

A numerical scheme employing a control volume approach was employed to discretize the governing equations to obtain finite volume equations. These equations were solved by the widely used

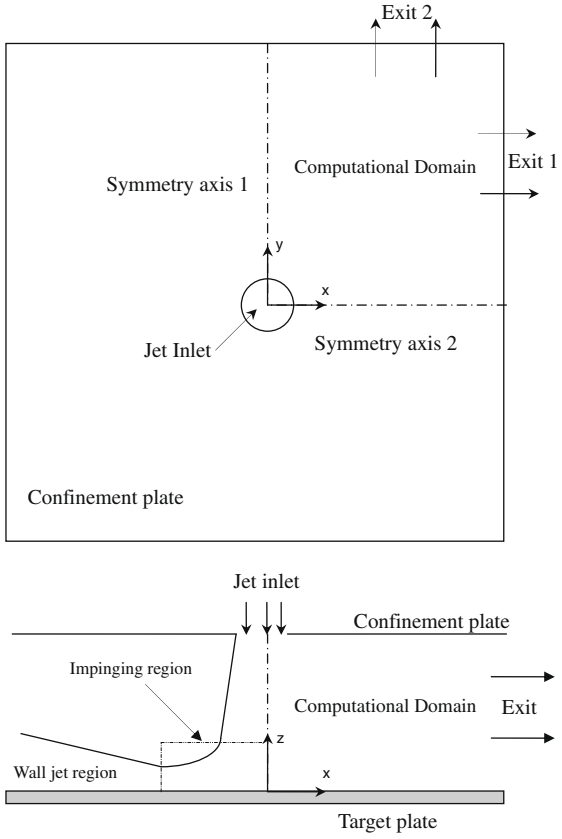

Fig. 1. Computational domain employed in the simulations.

CFD package PHOENICS, employing the SIMPLEST algorithm [13] for the pressure correction process along with the solution procedure for the hydrodynamic equations. The package uses staggered grid arrangement. For the discretization of convective-diffusive transport, the hybrid-scheme is the default scheme within the code. This scheme combines the stability of upwind-scheme with the approximate accuracy of the central-difference scheme. In the hybrid-scheme diffusion is cut off when the cell Peclet number ($Pe = Re\ Pr$, i.e. the ratio of heat convection to heat conduction) equals 2. In other words, the convective transport is assumed to dominate diffusive transport, and the hybrid-scheme reduces to the upwind formulation, with diffusion terms being neglected. The central-difference scheme leads to a second-order truncation error in the approximations, whereas the upwind-scheme gives only first order accuracy.

2.4. Boundary conditions

Fig. 1. shows the actual computational domain and the boundaries. No slip condition was accommodated along the solid walls and flow velocities were set to zero. Constant heat flux condition was applied at the target plate and 3 mm thick confinement plate in the solution domain was considered to be adiabatic. The other applied boundary conditions were as given below.

Target plate: q_c = constant

Inlet: W_{in} = specified, T_j = specified

Symmetry axis 1 and Outlet 1: x derivatives of the velocity components and temperature are set to zero:

$$\frac{\partial u}{\partial x} = 0, \quad \frac{\partial v}{\partial x} = 0, \quad \frac{\partial w}{\partial x} = 0, \quad \frac{\partial T}{\partial x} = 0 \tag{6}$$

Symmetry axis 2 and Outlet 2: y derivatives of the velocity components and temperature are set to zero:

$$\frac{\partial u}{\partial y} = 0, \quad \frac{\partial v}{\partial y} = 0, \quad \frac{\partial w}{\partial y} = 0, \quad \frac{\partial T}{\partial y} = 0 \tag{7}$$

2.5. Convergence, grid independency and comparison with experimental results

The PHOENICS code iteratively solves linear algebraic equations resulting from the finite volume integration of the partial differential equations. Due to the iterative process of the code, convergence was used as the monitor of achievement of the final solution. The criterion of convergence of the numerical solution is based on the absolute normalized residuals of the equations that were summed for all cells in the computational domain. Convergence was considered as being achieved when these residuals become less than 10^{-7}, which was the case for most of the dependent variables. Iterative convergence was also checked by terminating the solution only when the progressive single cell values of pressure, velocity and temperature showed little change per iteration as the calculation progressed. Furthermore, checks for the achievement of a final solution were made based on the conservation of mass, momentum and energy. Spot values were also controlled. Trial solutions were obtained with a wide range of cell number combinations for grid independency checks. Final simulations were performed with cell numbers ranging from $40 \times 40 \times 30$ to $40 \times 40 \times 64$ in the x-y-z coordinate directions depending on the jet to plate distance. Grids were refined in the jet region and close to the target surface. Extended boundary solutions were obtained to validate zero gradient velocity profiles at the exits. From these studies it was determined that additional extension of actual physical boundaries was not necessary, and did not affect the solutions. The computational domain and grid distribution is shown in the Fig. 2.

To validate the numerical solution, results of an experimental study conducted by Koseoglu [14] to determine the local heat transfer characteristics of impinging jets for different jet exit geometries, by using liquid crystals have been used. Comparison of experimental and numerical results in terms of local Nu numbers is shown in Fig. 3. Present model overpredicts the stagnation region heat transfer, but good agreement has been obtained in the wall jet region.

3. Experimental set-up and data reduction

Information on the experimental apparatus, devices used and procedures followed were given in detail by Koseoglu [14]. A summary of that information is presented below.

3.1. Experimental set-up

Schematic representation of the experimental set-up is shown in Fig. 4. The whole assembly including 3-D traverse system, target plate assembly, jet plate, plenum, and blower were fixed on a table for rigidity purposes. The required flow rate has been supplied by a centrifugal blower. In order to obtain the desired flow rate for the range of Re numbers of interest a frequency controller (SIEMENS, CINAMICS G110) has been connected to the blower. The rest of the set-up has been acoustically isolated from the blower with flexible hosing and dampers. Velocity measurements were made with a DANTEC 2-D LDA system. The system operates in backscatter mode and is used in conjunction with a 300 mW Argon Ion laser. The blower was connected to the plenum with a pipe of 900 mm length and 20 mm inner diameter. A hole was drilled through the pipe at a distance of 800 mm from the blower. This hole can be used to insert a hot wire anemometer (TSI 8345) to measure the velocities that can be used to double check the velocities which are obtained by using the 2-D LDA system.

Air is carried to the plenum through the connecting pipe from the blower. Plenum made of 10 mm thick Plexiglas is an 800 mm long rectangular duct with an inner square cross section of 100×100 mm. Portion (200 mm) of lower end section of the

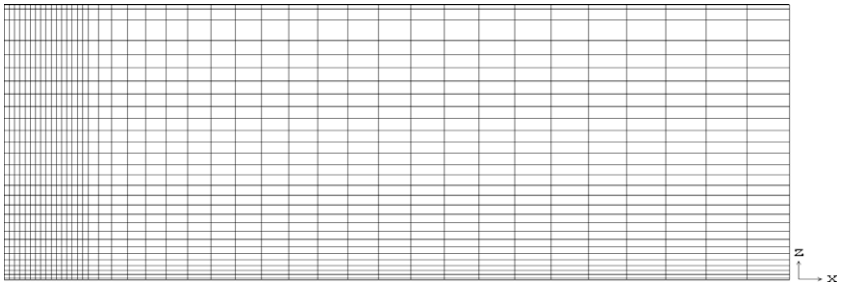

Fig. 2. Grid distribution in the x–z plane for dimensionless jet to plate distance 2.

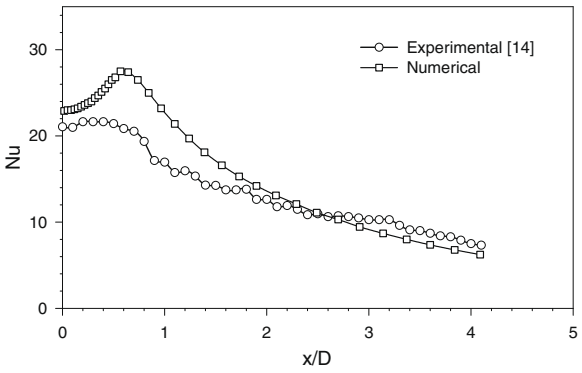

Fig. 3. Comparison of numerical and experimental results for $Re = 1000$ and $H/D = 2$.

plenum was cut off to easily mount and demount the orifice plates containing the jet. In order to measure the plenum air pressure and temperature two holes were drilled at approximately 550 mm from the plenum inlet to insert a static pressure tab and a T-type thermocouple. A sharp edged orifice type jet with a diameter of 10 mm was drilled on a $200 \times 120 \times 3$ mm orifice plate by laser cutting technique with centers located at 50 mm from the sides and from the end of the plenum. In the experiments a uniform flow was achieved at the jet exit. To satisfy this condition, flow was almost brought to rest in the large plenum prior to the jet exit. In addition to that, orifice plate thickness was limited to 3 mm to prevent flow development which could damage uniform flow conditions.

During the determination of the jet inlet velocity with the LDA system, measurements have been taken starting from the jet centerline to the jet edge. Despite thin orifice plates, to prevent the flow development, close to the jet edge lower velocities have been obtained. This is an indication of the flow to be different than a plug flow. It could be because of the sharp edges of the orifices, size of the LDA measurement volume, and plenum chamber. In the experimental part the main goal was to determine the effect of natural convection on average heat transfer. The wall jet region comprises a very large portion of the plate, so the effect of the above mentioned deviation in the velocity profile on the average heat transfer is considered to be negligible, in terms of the goals of experimental research.

The target plate assembly consists of target plate, resistance heater, thermocouples, insulation and traverse mechanism (Fig. 4). Target plate material is copper with dimensions of $100 \times 100 \times 5$ mm. Copper has been chosen as target plate material because of its high thermal conductivity which is ideal for determination of average Nusselt numbers. Resistance heater of thickness 2 mm was placed at the back of the plate. The total power supplied was controlled by a voltage transformer and an AC power meter (GWINSTEK-GPM8212). Target plate was equipped with 19, 30-gauge copper-constantan thermocouples inserted along the center of the plate at 5 mm intervals. Thermocouples were inserted through holes of 1.5 mm diameter machined through 4.8 mm thickness of the plate from the bottom and fixed with thermal adhesive (Arctic Silver 5). Two layers of material were used to insulate the backside of the target plate and the heater assembly. The first layer was glass wool (Izopan) insulation of 15 mm and on top of that 60 mm of Styrofoam insulation was applied. In addition, the target plate was insulated at the sides with pure Teflon (PTFE) of 5 mm thickness. The above mentioned target plate, heater and insulations were placed in a Styrofoam skeleton and metal box. In order to calculate heat losses from the insulation assembly, inner and outer walls of the assembly at the bottom and sides were equipped with a total of 10 thermocouples. All thermocouples were separately calibrated. Signals from the thermocouples were collected, processed, stored, and analyzed with a data acquisition system (Agilent 34980A). The whole target plate assembly was fixed on a 3-D traverse system which was used to set the desired jet to target plate distance.

3.2. Processing of the experimental data

Experimental data were reduced in terms of average heat transfer coefficient and Nusselt number. In these calculations the convective heat transfer rate was calculated from an energy balance as given below:

$$Q_c = Q_t - Q_r - Q_{\text{cond}} \tag{8}$$

First the total power dissipation from the resistance heater was determined from

$$Q_t = VI \tag{9}$$

where V is the voltage drop across the heater and I is the measured current. From this total power dissipation, Q_c was calculated by subtracting losses due to radiation (Q_r) from the target plate and conduction (Q_{cond}) from the bottom and sides. Conduction losses were obtained from a one dimensional conduction analysis through the insulation thicknesses by using measured temperatures at the inner and outer surfaces. Radiation heat losses were calculated from:

$$Q_r = \varepsilon\sigma F A_s (T_{s,\text{ave}}^4 - T_\infty^4) \tag{10}$$

where the view factor between the target plate and its surroundings was taken to be unity and the surface emissivity was measured to be 0.04. A_s is the surface area of the target plate, temperature of the surroundings (T_∞) was taken to be the room temperature. Average surface temperature ($T_{s,\text{ave}}$) was obtained from the arithmetic mean of 19 thermocouple readings. Due to the very high thermal

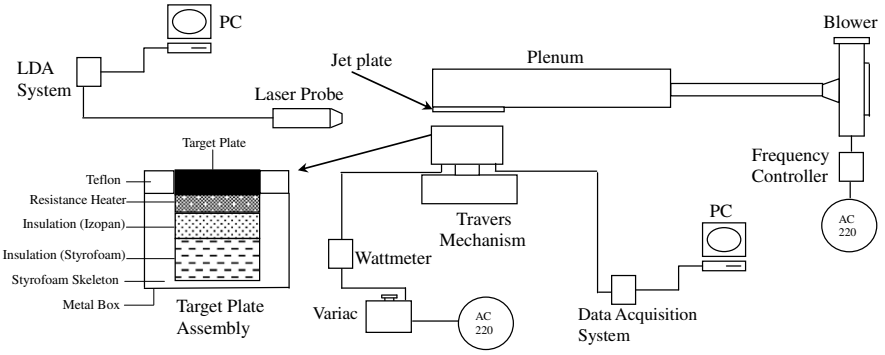

Fig. 4. Schematic diagram of the experimental set-up and target plate assembly.

Table 1
Measurement uncertainties

Variable	Uncertainty (%)
Q_t	2%
Q_{cond}	4,87%
Q_r	24,66%
Q_c	2,2%
h_{ave}	4,35%
Nu_{ave}	4,4%
Gr^*	3,68%
Re	2,23%
Ri	5,74%

conductivity of the copper target plate, all temperature readings were very close to each other and an almost uniform temperature distribution was obtained. Maximum difference between thermocouple readings was around 1 °C for the worst case.

By using the convection heat transfer rate the average convection heat flux can be calculated as follows:

$$q_c = \frac{Q_c}{A_s} \tag{11}$$

Hence, the average heat transfer coefficient is defined as:

$$h_{ave} = \frac{q_c}{(T_{s,ave} - T_j)} \tag{12}$$

where T_j is the jet inlet temperature. Finally the average Nusselt number is given as below:

$$Nu_{ave} = \frac{h_{ave} D}{k_{air}} \tag{13}$$

where D is the jet diameter and k_{air} is the thermal conductivity of air.

Other dimensionless numbers affecting the heat transfer are given below:

The Reynolds number:

$$\mathrm{Re} = \frac{W_{in} D}{\nu_{air}} \tag{14}$$

The modified Grashof number:

$$Gr^* = \frac{g\beta q_c L^4}{k_{air}\nu_{air}^2} \tag{15}$$

The Richardson number:

$$Ri = \frac{Gr^*}{Re^2} \tag{16}$$

Thermophysical properties were evaluated at the average of jet inlet and plate temperatures, except for the viscosity in the *Re* number which was calculated at the jet inlet temperature.

In order to determine the reliability of the experimental results, an uncertainty analysis was conducted on all measured quantities as well as the quantities calculated from the measurement results. Uncertainties were estimated according to the standard procedures reported in the literature; see e.g. Moffat [15,16], Abernethy et al. [17], Kline [18], Smith Jr. and Wehofer [19]. Overall, the uncertainty in the Nusselt number is around 4–5%. Uncertainties in the other calculated variables are shown in Table 1.

4. Results and discussion

The influence of buoyancy effects on confined impinging jet heat transfer has been investigated experimentally and numerically. In this part first numerical results regarding local heat transfer and then experimental results on average heat transfer under various conditions are presented. The values of parameters corresponding to these conditions are of 250–5000 for the Reynolds number, and 2–12 for the dimensionless jet to plate distance at modified Grashof numbers between 22900 and 2586000. In the presented figures "forced" case represents the solution for local Nusselt number distribution where the buoyancy term is neglected in the governing equations.

In Fig. 5 local Nusselt number distributions on the plate as a function of dimensionless distance (x/D) from the impinging point are presented for $Re = 250$, $H/D = 2$, 4, 8, 12 and various Grashof numbers. As can be seen from these figures, for all jet to plate distances different heat transfer characteristics have been observed depending on the Grashof number. For $H/D = 2$, at the impinging region and at the beginning of the wall jet region, natural convection effects are not visible even for the highest Gr^* number which corresponds to the maximum heat flux applied. With decreasing jet velocity at the far wall jet region forced convection effects reduce and heat transfer enhancement associated with buoyancy induced flow evolves. This assisting buoyancy effect occurred for the highest Gr^* number at the shortest distance from the impinging point at around $x/D = 2.5$, at lower Grashof numbers, the same effect is visible at later positions.

For dimensionless jet to plate distances 4 and 8, prior to assisting buoyancy induced flow in the wall jet region, an opposing effect of buoyancy induced upward flow is clearly observed in the impinging region especially at high Gr^* numbers. In the wall jet region, flow parallel to the target plate, as a result of the forced convective fluid flow nature of the jets, is slowed down by the buoyancy induced upward flow. As a result, from the stagnation point onwards a more dramatic decrease in the Nusselt number is observed at increasing Gr^* numbers depending on the jet to plate distance and the strength of the upward flow.

At $H/D = 12$, previously mentioned opposing and assisting natural convection effects continue to affect the heat transfer in an increasing manner. In addition, on the impinging point buoyancy induced upward flow even hinders the down coming jet, which is already slowed down because of the increased jet to plate distance. At $H/D = 12$ the plate distance is longer than the potential core length. After the jet reaches the plate and becomes a wall jet, from that point on natural convection effects are observed on the whole plate. At the two highest Gr^* numbers, assisting natural convection effects are observed on the whole plate.

At $Re = 500$, for all jet to plate distances the starting point of assisting buoyancy induced flow shifts toward the outer edge of the target plate (Fig. 6). Previously mentioned opposing buoyancy effect before the onset of assisting flow is still present but somehow diminished. From the maximum heat transfer point on a sharper drop in the Nusselt number for increasing Gr^* numbers is observed. At dimensionless jet to plate distance 12, buoyancy induced upward flow at stagnation point is still able to slow down the jet at the highest Gr^* number but it is not strong enough to prevent the jet reaching the plate. As a result of this slowing down of the jet, stagnation point heat transfer at this Gr^* number is lower than the others.

For the *Re* number of 1000, because of the increased jet inlet velocity, absolute magnitudes of local *Nu* numbers and forced convection effects are increased. As a result of this, buoyancy induced effects are almost completely diminished. Opposing effect of buoyancy induced upward flow in the stagnation and wall jet region almost disappeared except for the highest Gr^* number (Fig. 7).

From the numerical results, it has been shown that buoyancy induced natural convection could have opposing or assisting effects on local Nusselt numbers, at different locations on the target plate, depending on H/D, Re and Gr^* numbers. As an example from a large number of typical velocity vector distributions, Fig. 8 shows the distributions in the flow field for two different Gr^* numbers at

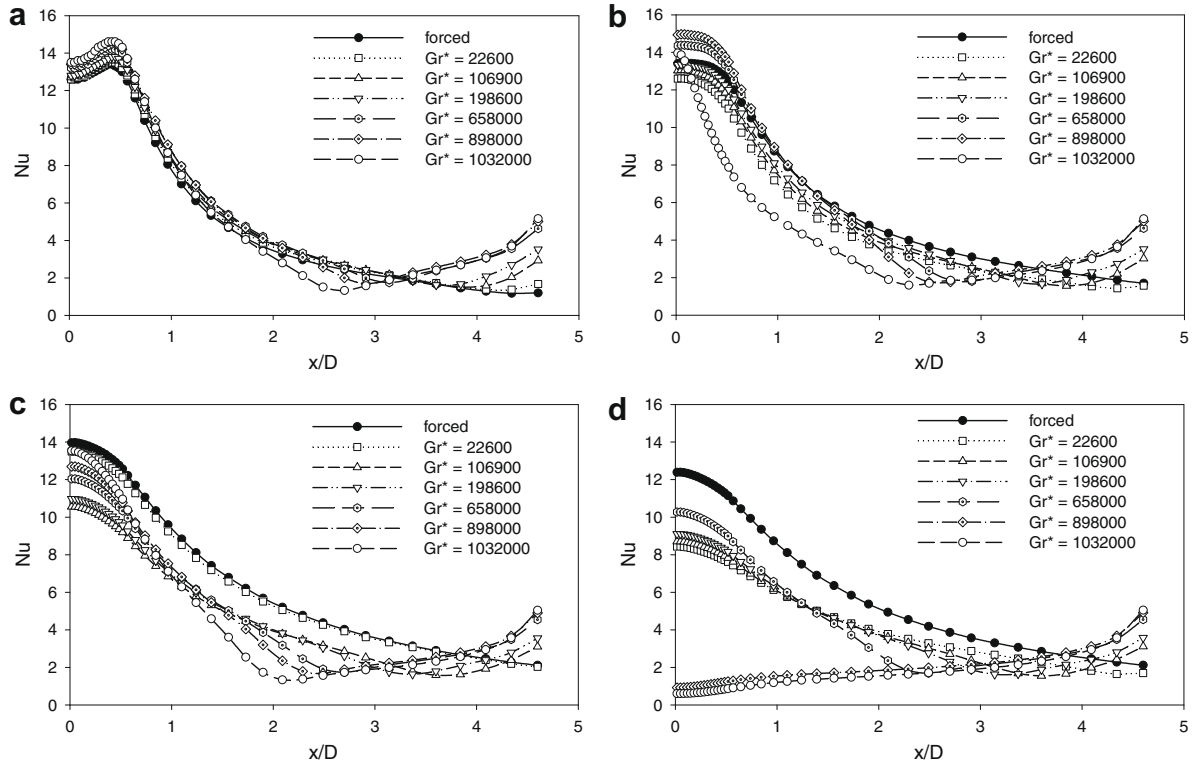

Fig. 5. Effect of Grashof number on local Nusselt number at $Re = 250$ for (a) $H/D = 2$, (b) $H/D = 4$, (c) H/D = 8, (d) $H/D = 12$.

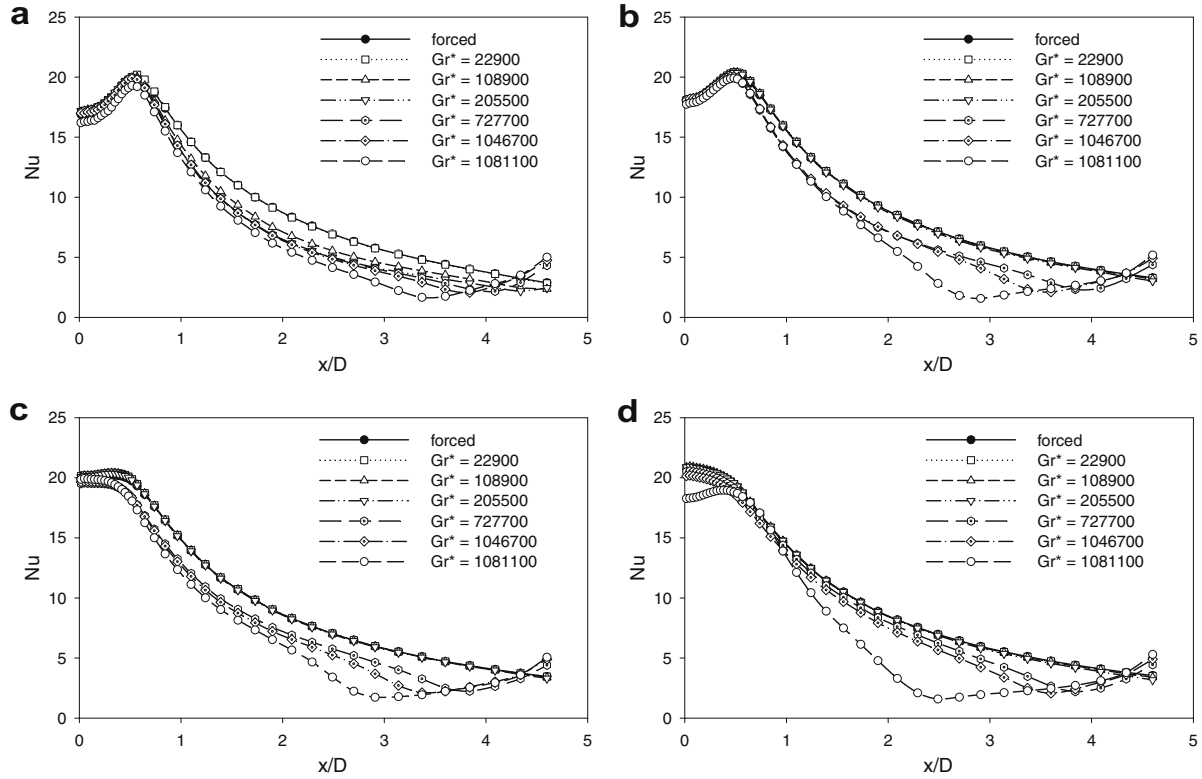

Fig. 6. Effect of Grashof number on local Nusselt number at $Re = 500$ for (a) $H/D = 2$, (b) $H/D = 4$, (c) $H/D = 8$, (d) $H/D = 12$.

$Re = 250$, comparing the cases with and without natural convection effects. Effect of buoyancy induced natural convection on the flow field at increasing Gr^* number is clearly visible. At $Gr^* = 1{,}032{,}000$ in the impinging and even in the free jet region, the downwards flowing jet is slowed down by upward natural convection currents. An opposing effect of buoyancy induced natural convection on the

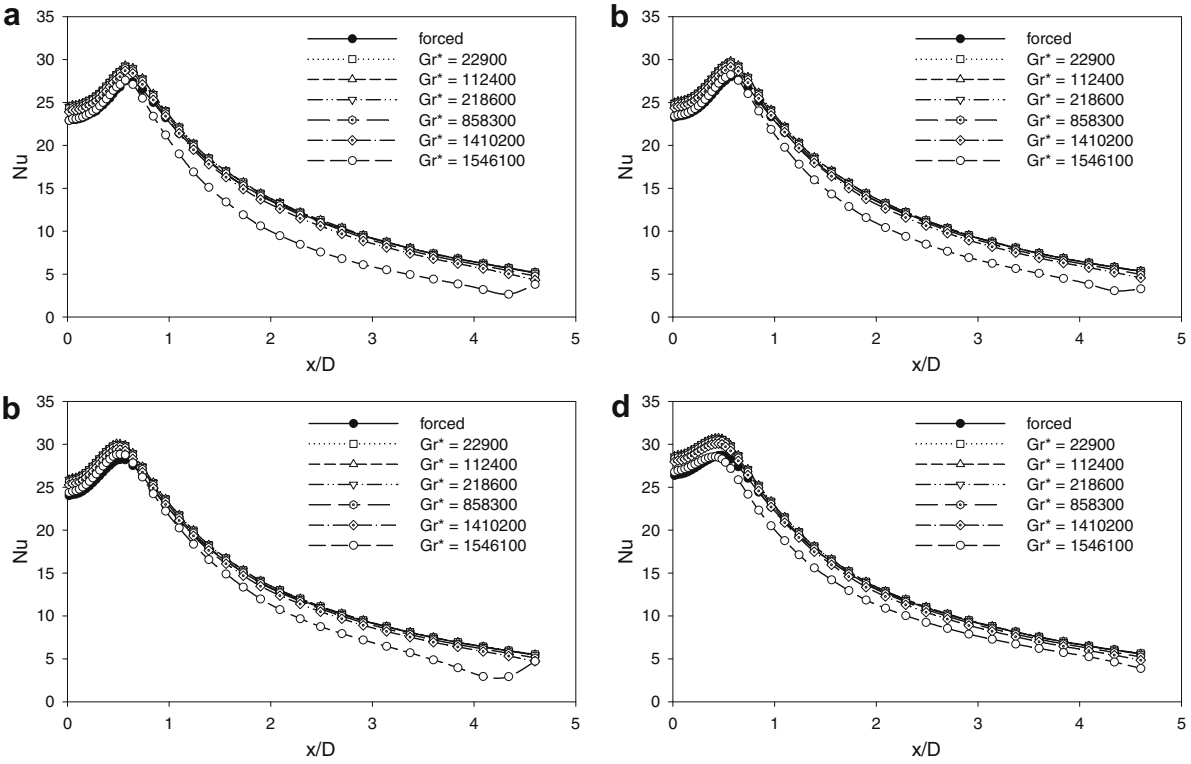

Fig. 7. Effect of Grashof number on local Nusselt number at $Re = 1000$ for (a) $H/D = 2$, (b) $H/D = 4$, (c) $H/D = 8$, (d) $H/D = 12$.

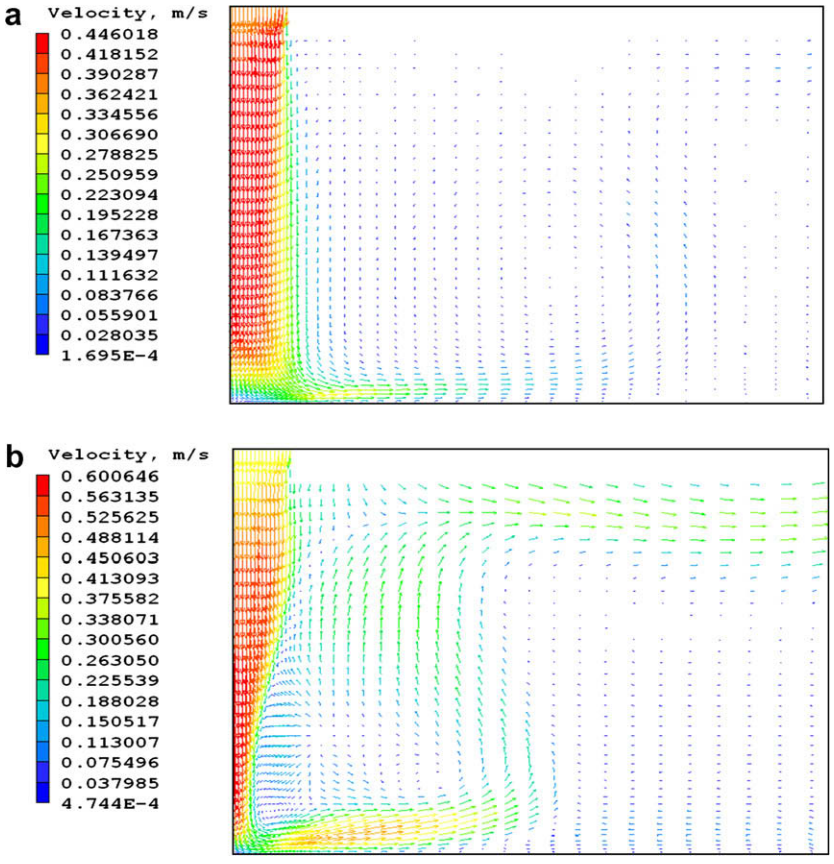

Fig. 8. Velocity vector distribution in the flow field at $Re = 250$, $H/D = 4$: (a) $Gr^* = 22600$, (b) $Gr^* = 1032000$.

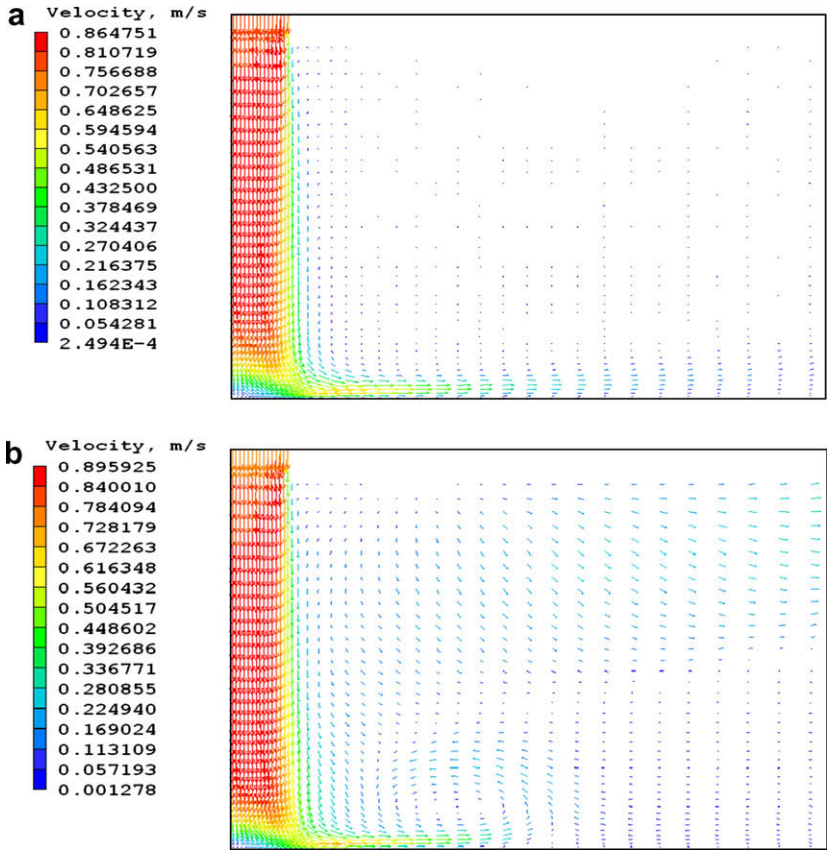

Fig. 9. Velocity vector distribution in the flow field at $Re = 500$, $H/D = 4$: (a) $Gr^* = 22900$, (b) $Gr^* = 1081100$.

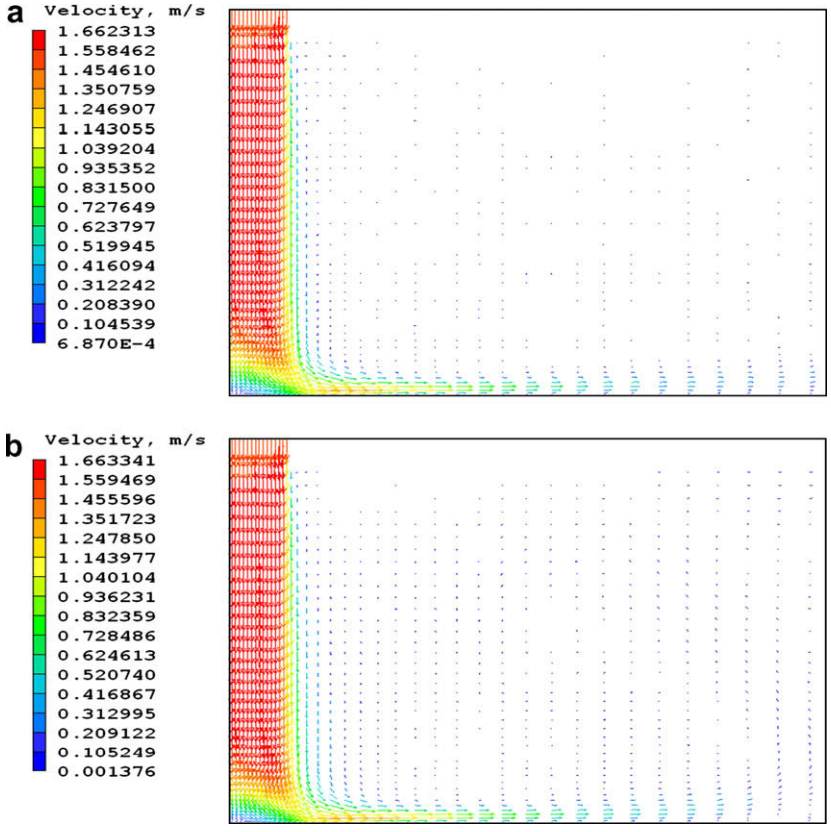

Fig. 10. Velocity vector distribution in the flow field at $Re = 1000$, $H/D = 4$: (a) $Gr^* = 22900$, (b) $Gr^* = 1546100$.

wall jet is also observed. This effect slows down the jet and hinders the wall jet development, causing a small recirculation region. After that point on, assisting natural convection dominates the flow. Bouyancy induced effects diminishes with increasing Reynolds number. Figs. 9 and 10 show the flow field for Reynolds numbers 500 and 1000 respectively. At $Re = 500$ effect of increasing Grashof number is visible in the wall jet region but at $Re = 1000$, flow profiles at the lowest and highest Grashof numbers are very similar.

In order to determine the overall effect of natural convection on the average heat transfer, experiments have been conducted at dimensionless jet to plate distances 2, 4, 8 and 12, and Re numbers in the range of 250–5000 for various Gr^* numbers, and these experimental results and comparison with conjugate numerical solutions were presented in Figs. 11–16. The results of the experimental study are presented using the modified Gr^* number based on heat flux and jet to plate distance.

In Fig. 11, average Nusselt numbers are presented for $Re = 250$, 500, 750 as a function of Gr^* number for different jet to plate distances. For $Re = 250$ and 500 average Nusselt number increases with increasing Gr^* number at every dimensionless jet to plate distance except for $Re = 500$ and $H/D = 12$. Buoyancy induced assisting flow, which was also observed from the numerical results in the wall jet region after $x/D = 2.5$ covering a very large portion of the square target plate, dominates the opposing effect and higher average Nusselt numbers are obtained. At $Re = 250$ and 500, the highest average Nusselt number corresponding to the highest Gr^* number is obtained at $H/D = 4$. Although, it is not as strong as before, above mentioned assisting buoyancy induced flow effects are still visible at $Re = 750$.

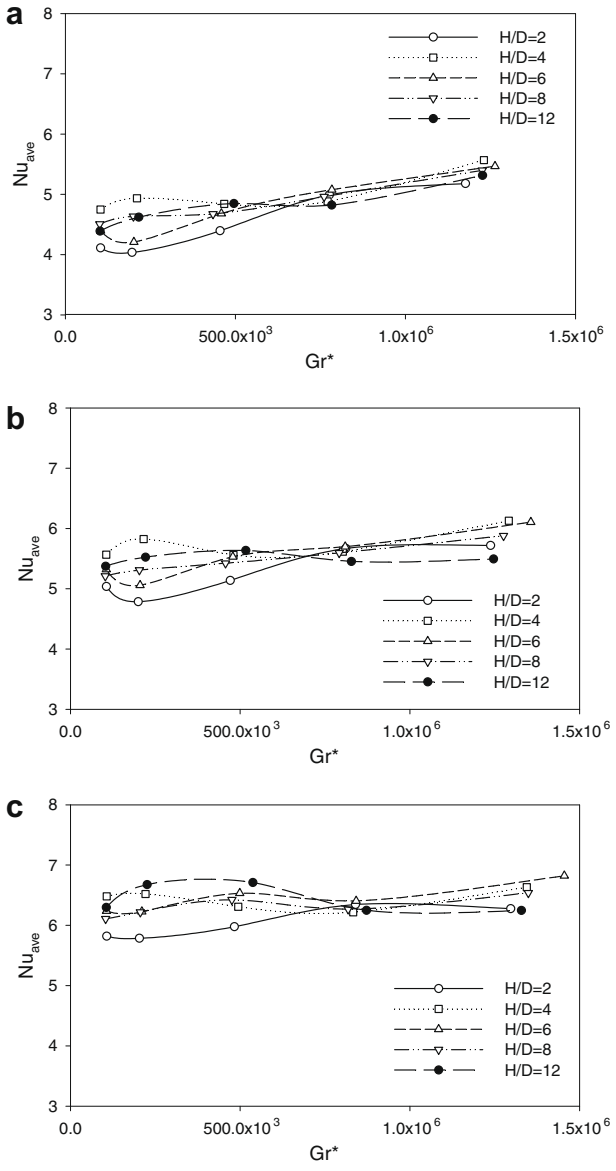

Fig. 11. Effect of Grashof number and jet to plate distance on average Nusselt number for (a) $Re = 250$, (b) $Re = 500$, (c) $Re = 750$.

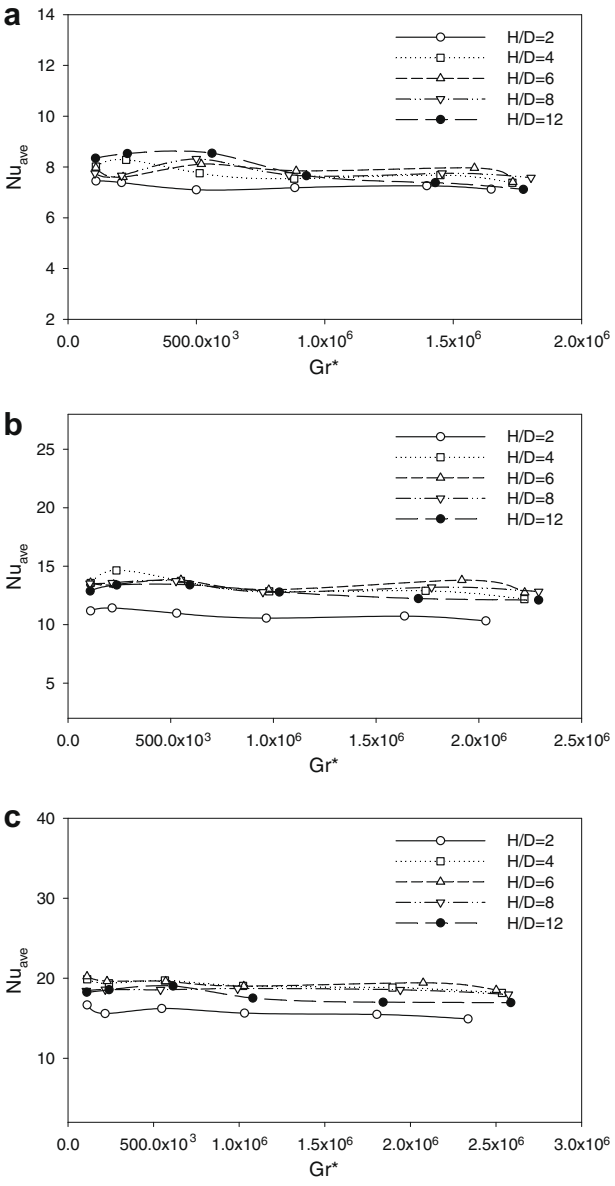

Fig. 12. Effect of Grashof number and jet to plate distance on average Nusselt number for (a) $Re = 1000$, (b) $Re = 3000$, (c) $Re = 5000$.

Fig. 12, shows average Nusselt numbers as a function of Gr^* number for Re numbers 1000, 3000, 5000. With increasing Re number, affect of forced convection on the total heat transfer rate increases. As a result of this, buoyancy effects on the total average heat transfer do not occur at $Re = 3000$ and 5000 even for the highest Gr^* number tested.

Conjugate numerical solutions were also obtained for average heat transfer at increasing Grashof numbers. Fig. 13, shows the

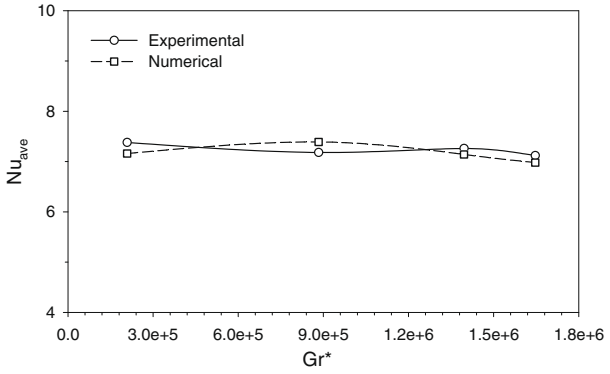

Fig. 13. Effect of Grashof number on average Nusselt number, comparison of numerical and experimental results for $Re = 1000$, $H/D = 2$.

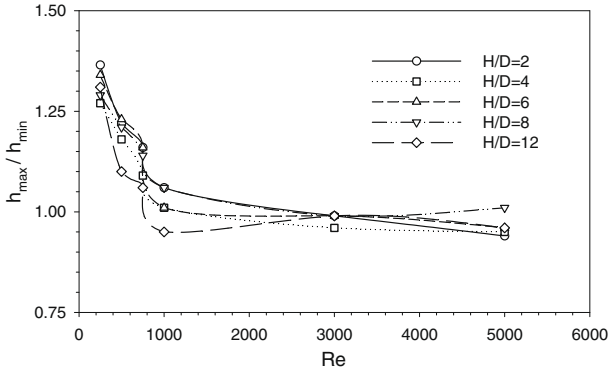

Fig. 16. Increase in average heat transfer coefficient due to natural convection effects.

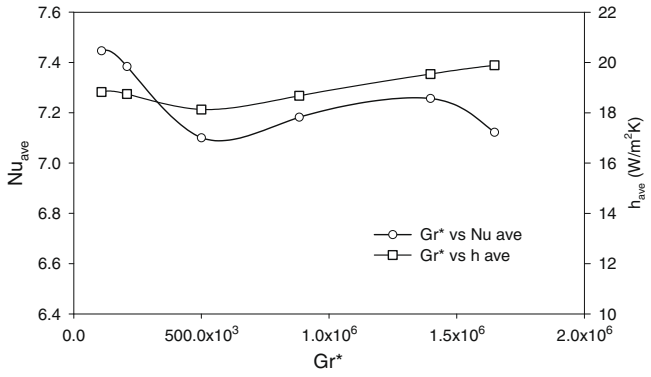

Fig. 14. Effect of Grashof number on average Nusselt number and heat transfer coefficient for $Re = 1000$ and $H/D = 2$.

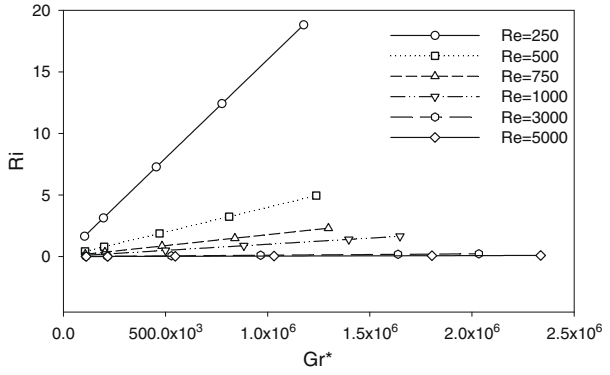

Fig. 15. Change of Richardson number as a function of Gr* and Re number for $H/D = 2$.

comparison between experimental and numerical results for $Re = 1000$. As can be seen, the conjugate model predicts the average heat transfer rate quite well.

At $Re = 1000$ there seems to be a decrease in average Nusselt number with increasing Gr^* number. But when the average heat transfer coefficient is drawn as a function of Gr^* number this is not the case (Fig. 14). This seems to be a contradiction, but it results because of the increase of thermal conductivity with temperature, which is calculated at the average of plate surface and jet temperature in the average Nu number calculation.

Richardson number is an indication of relative importance of natural and forced convection. Fig. 15 shows the Richardson number as a function of Gr^* number for all investigated Re numbers. Incropera and Dewitt [20] stated that natural and forced convection effects should be considered together when the Richardson number is around or greater than unity. It is seen in the figure that at $Re = 250$, 500, 750 and 1000 natural convection effects are considerable and should be taken into account in heat transfer calculations.

Effect of buoyancy induced flow on the average heat transfer rate mainly depends on Re and Gr^* numbers. Fig. 16 shows the ratios of average heat transfer coefficient obtained for the highest Gr^* number and the value of it obtained at the lowest Gr^* number at which natural convection effects are negligible. It is seen that at $Re = 250$ and $H/D = 2$, 37% percent increase on the average heat transfer coefficient is obtained. At other jet to plate distances enhancements between 25% and 35% is observed. At $Re = 500$ and 750 highest enhancement is obtained at $H/D = 6$ with 24% and 17% respectively. For $Re = 1000$, 3000, 5000 because of the very dominant forced convection very little change is observed in the average heat transfer coefficient with increased Gr^* number.

5. Conclusions

The influence of natural convection on the local and average heat transfer at increasing temperature differences between the jet and the target plate from confined impinging jets has been experimentally and numerically investigated. The values of parameters under investigation were 250–5000 for the Reynolds number, 2–12 for the dimensionless jet to plate distance, and 22,900–2,586,000 for the modified Gr^* number.

From the numerical results, it has been shown that buoyancy induced natural convection could have opposing or assisting effect on local Nusselt numbers at different locations on the target plate. With decreasing jet velocity, in the wall jet region, forced convection effects drop and heat transfer enhancement associated with buoyancy induced flow occurs. Prior to assisting buoyancy induced flow in the wall jet region, opposing effect of buoyancy induced upward flow is observed very clearly especially at high Gr^* numbers. In this region, jet flow parallel to the target plate is slowed down by the buoyancy induced upward flow. As a result, from the stagnation point onwards a more dramatic decrease in the Nusselt number is observed at increasing Gr^* numbers depending on the strength of the upward flow. It has been determined that at Re = 250, 500, 750 and partly at 1000 natural convection has an increasing influence with increasing Grashof number on the average heat transfer. This influence should be taken into account in the heat transfer analysis. Finally, one can say that as a result of buoyancy induced natural convection currents,

experimental average heat transfer rate can be increased approximately up to 37%.

Acknowledgements

Financial support of this study by the research fund of the Gazi University under Grant No. BAP 06/2005-51 and State Planning Organization of Turkey under Grant No. DPT-2003K120470-28 is gratefully acknowledged.

References

[1] R. Viskanta, Heat transfer to impinging isothermal gas and flame jets, Exp. Therm. Fluid Sci. 6 (1993) 111–134.
[2] K. Jambunathan, E. Lai, M.A. Moss, B.L. Button, A review of heat transfer data for single circular jet impingement, Int. J. Heat Fluid Flow 13 (1992) 106–115.
[3] R. Gardon, J.C. Akfirat, The role of turbulence in determining the heat transfer characteristics of impinging jets, Int. J. Heat Mass Transfer 8 (1965) 1261–1272.
[4] R. Gardon, J.C. Akfirat, Heat transfer characteristics of impinging two dimensional air jets, J. Heat Transfer 88 (1966) 101–108.
[5] S.V. Garimella, Heat transfer and flow fields in confined jet impingement, Ann. Rev. Heat transfer 11 (1999) 413–494 (Chapter 7).
[6] I. Sezai, A.A. Mohamed, Three dimensional simulations of laminar rectangular impinging jets, flow structure and heat transfer, ASME J. Heat Transfer 121 (1999) 50–56.
[7] S.Z. Shuja, B.S. Yilbas, M. Rashid, Confined swirling jet impingement onto an adiabatic wall, Int. J. Heat Mass Transfer 46 (2003) 2947–2955.
[8] M.H. Yu, P.A. Monkewitz, Oscillations in the near field of a heated two dimensional jet, J. Fluid Mech 255 (1993) 323–347.
[9] Y. Shi, A.S. Mujumdar, M.B. Ray, Effect of large temperature difference on impingement heat transfer under a round turbulent jet, Int. Comm, Heat Mass Transfer 31 (2004) 251–260.
[10] L.A. Brignoni, S.V. Garimella, Effects of nozzle-inlet chamfering on pressure drop and heat transfer in confined air jet impingement, Int. J. Heat Mass Transfer 43 (2000) 1133–1139.
[11] D. Lytle, B.W. Webb, Air jet impingement heat transfer at low nozzle-plate spacing, Int. J. Heat Mass Transfer 37 (1994) 1687–1697.
[12] D. Gray, A. Giorgini, The validity of the Boussinesq approximation for liquids and gases, Int. J. Heat Mass Transfer 19 (1976) 545–551.
[13] D.B. Spalding, The PHOENICS Encyclopedia, London.
[14] M.F. Koseoglu, Experimental and numerical investigation of electronics equipment cooling with impinging jets, Ph.D. Thesis, Gazi University, Ankara, Turkey, 2007.
[15] R.J. Moffat, Contributions to the theory of single-sample uncertainty analysis, J. Fluids Eng. 104 (1982) 250–260.
[16] R.J. Moffat, Using uncertainty analysis in the planning of an experiment, J, Fluids Eng. 107 (1985) 173–178.
[17] R.B. Abernethy, R.P. Benedict, R.B. Dowdell, ASME measurement uncertainty, J. Fluids Eng. 107 (1985) 161–164.
[18] S.J. Kline, The purposes of uncertainty analysis, J. Fluids Eng. 107 (1985) 153–160.
[19] R.E. Smith, S. Wehofer Jr., From measurement uncertainty to measurement communications, credibility, and cost control in propulsion ground test facilities, J. Fluids Eng. 107 (1985) 165–172.
[20] F.P. Incropera, D.P. DeWitt, Fundamentals of Heat and Mass Transfer, fourth ed., Wiley, Newyork, 1996.